Induction Pump for High-Temperature Molten Metals Using Rotating Twisted Magnetic Field: Molten Gallium Experiment

Tsutomu Ando, Kazuyuki Ueno, Shoji Taniguchi, and Toshiyuki Takagi, *Member, IEEE*

***Abstract*—We report a study of an electromagnetic pump, applicable to processing high-temperature molten metal such as molten steel at over 1500 °C. A rotating twisted magnetic field is generated by a stator with three pairs of helical windings. Axial thrust, as well as rotational torque, acts on the molten metal in cylindrical ducts. We carried out a molten metal circulation experiment using molten gallium at 50 °C and confirmed that the conventional slip-thrust relation is satisfied in the experiment. Here, we identify the slip for each experimental condition and discuss the motion of molten gallium in the rotating twisted magnetic field. The normalized stalling pressure is obtained at the frequency at which $\delta/a_2 \approx 0.6$, where δ is the skin depth and a_2 is the radius of molten metal.**

***Index Terms*—Electromagnetic devices, electromagnetic forces, electromagnetic processing of metals, electromagnetic pump, induction machines, magnetohydrodynamics.**

I. Introduction

RECENTLY, applications of electromagnetic forces have been developed in the steelmaking process, where stable performance in a harsh environment is required [1], [2]. The development of an induction electromagnetic pump is expected in that process because, in maintainability and durability, electromagnetic induction pumps are superior to mechanical pumps and electromagnetic dc pumps. Direct action of the electromagnetic force with neither impellers nor electrodes results in a simple design with fewer parts that can be damaged. Until now, however, there has been no electromagnetic pump that can actually be used with high-temperature molten metals, for example, molten steel at over 1500 °C.

The annular linear induction pump (ALIP) is one of the most familiar conventional induction pumps [3], [4]. It has an iron core installed in the duct so that the magnetic field may traverse the working fluid. However, the iron core loses its ferromagnetic property when its temperature is higher than its Curie point. Moreover, pillars that support the iron core are seriously damaged by high temperatures. As a result, the ALIP cannot be used with high-temperature molten metals.

In this paper, an electromagnetic induction pump for material processing is studied. The stator of this machine generates a rotating twisted magnetic field by means of a helical coil [5]. Since this helical coil enables the magnetic field to penetrate the center of the duct, this magnetohydrodynamic (MHD) pump does not need an iron core in the duct, which is consequently a simple structure. Since we do not need to carry out any machining on the ducts, we can make the duct from various materials with special properties such as heat resistance and corrosion resistance. Moreover, since this magnetic field gives axial thrust as well as rotational torque to the secondary conductor, this machine has both properties of the linear pump and the rotary stirrer.

The authors have already reported the results of experiments with a solid secondary conductor (bulk rotor) in previous papers [6], [7]. It was verified that thrust was obtained using a rotating twisted magnetic field. And the authors also qualitatively confirmed that this machine works as a pump in a preliminary experiment [8].

This paper reports on a circulation experiment using molten gallium quantitatively. In the discussion, we report that the conventional slip-thrust relation is applicable to molten metal. We identify the slip of molten gallium with this relation and discuss the motion of molten gallium in a rotating twisted magnetic field.

II. Rotating Twisted Magnetic Field

Three pairs of helical windings, as shown in Fig. 1(b), were adopted in order to generate a rotating twisted magnetic field. It was an improved stator of an ordinary rotary induction motor [Fig. 1(a)]. If the stator is twisted, the windings are twisted together into a helical shape, as shown in Fig. 1(b). Since this coil has three-phase two-pole windings, the magnetic field rotates in the cross section (x–y plane) of the secondary conductor. Meanwhile, the direction of the field vector changes with z, because the winding is helical. This magnetic field rotates at a constant speed keeping the spatial distribution, as shown in Fig. 1(c).

The rotating twisted magnetic field travels along the z axis as well as rotating in x–y plane. This is a necessary property for obtaining the axial thrust. We draw an analogy between the rotating twisted magnetic field and impellers of axial-flow turbo

Manuscript received August 15, 2003; revised April 19, 2004. This work was supported in part by the Matsuda Foundation's Research Grant, the Casio Science Foundation's Research Grant, and the Ministry of Education, Culture, Sports, Science and Technology, Grant-in-Aid for Scientific Research in Priority Areas, no. 10211202. This work was supported in part by the Ministry of Education, Science, Sports and Culture, Grant-in-Aid for Young Scientists (A), no. 1474402053, 2003.

T. Ando is with the Tsukuba Magnet Laboratory, National Institute for Material Science, Ibaraki 305-0003, Japan (e-mail: Ando.Tsutomu@nims.go.jp).

K. Ueno is with the Department of Aeronautics and Space Engineering, Graduate School of Engineering, Tohoku University, Sendai 980-8579, Japan (e-mail: ueno@cfd.mech.tohoku.ac.jp).

S. Taniguchi is with the Graduate School of Environmental Studies, Tohoku University, Sendai 980-8579, Japan (e-mail: s-tanig@material.tohoku.ac.jp).

T. Takagi is with the Institute of Fluid Science, Tohoku University, Sendai 980-8577, Japan (e-mail: takagi@ifs.tohoku.ac.jp).

Digital Object Identifier 10.1109/TMAG.2004.831000

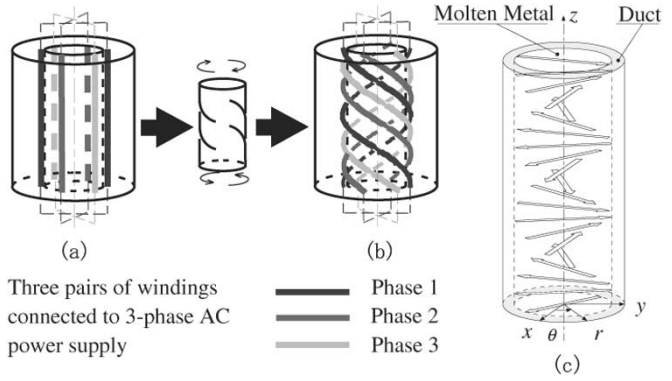

Fig. 1. Windings and magnetic field. (a) Stator of an ordinary three-phase two-pole induction motor. (b) Stator of the induction pump for high temperature molten metals: three pairs of helical windings. (c) Rotating twisted magnetic field.

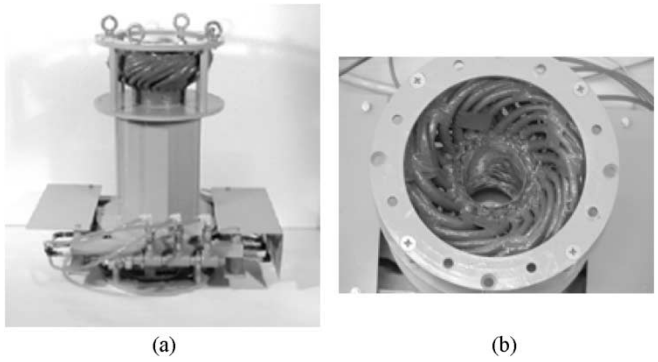

Fig. 2. Stator. (a) Side view. (b) Top view.

pumps, in which straight motion is caused by the rotation of twisted matter.

III. Experimental Apparatus

A. Stator

A prototype stator with three pairs of helical windings was fabricated for this molten gallium circulation experiment. A photograph of the stator is shown in Fig. 2. The exposed parts are connections of the coil end. The main specifications of this stator are shown in Table I. The twist angle of the coil means an angle between the z axis and windings. Eight-turn helical coils per phase are composed of 16 copper pipes with rectangular cross sections. The position of the windings in a cross section of the stator is shown in Fig. 3. Fig. 4 shows the inner and outer windings formed into a helical shape. This stator can continue to operate for long periods owing to water cooling.

B. Magnetic Flux Density

When a stator had teeth and slots, the distribution of the magnetic flux density of the stator had remarkable spatial higher harmonics corresponding to the teeth and slots [7]. Therefore, we removed the teeth of the yoke and integrated additional windings into this space.

Before manufacturing this stator, we calculated the magnetic flux density by numerical analysis to check the effect of the teeth. The details of this numerical analysis and the results are shown in Appendix I. This result shows that the magnetic flux density at the center of the stator without teeth was 22% higher than that with teeth and the uniformity was greatly improved.

TABLE I
Specification of the Stator

Inside diameter of helical coil	ϕ 80 mm
Outside diameter of helical coil	ϕ 125 mm
Outside diameter of yoke	ϕ 180 mm
Length of yoke	305 mm
Twist angle of the coil at ϕ 80 mm	39 °
Number of coil windings (N)	8 turn
Number of poles	2
Number of phases	3
Winding connection	Star

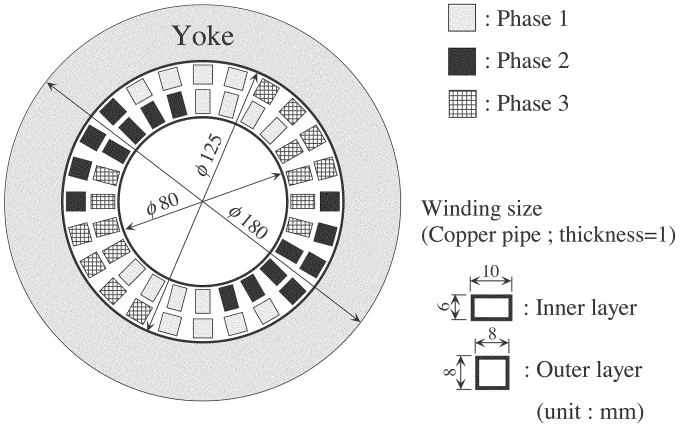

Fig. 3. Position of windings in a cross section of the stator.

Fig. 4. Inner and outer windings of spiral coil on manufacture.

TABLE II
CIRCUMFERENTIAL AVERAGE OF rms VALUES OF MAGNETIC FLUX DENSITY ON THE CROSS SECTION AT $z = 0$ mm WHEN $\bar{I} = 30$ A, $N = 8$, AND THE STATOR BORE IS EMPTY

	$r = 0$ mm	$r = 20$ mm		$r = 32$ mm	
	$\bar{B}_x = \bar{B}_y$ [mT]	$\bar{B}_r$ [mT]	$\bar{B}_\theta$ [mT]	$\bar{B}_r$ [mT]	$\bar{B}_\theta$ [mT]
Measurement†	4.5	4.5	4.4	5.0	4.6
Analysis‡	3.73	4.03	3.87	4.50	4.02

†Accuracy of the measuring instruments : ±0.6 mT.
‡These values are given by numerical analysis in Appendix I.

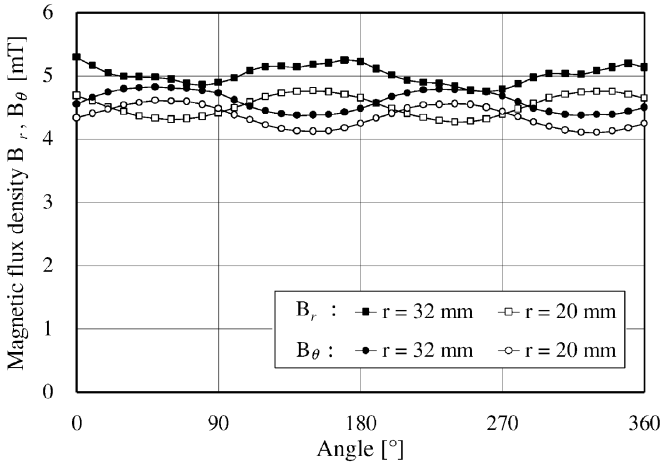

Fig. 5. Circumferential distribution of root-mean-square value $\bar{B}_r$, $\bar{B}_\theta$ of magnetic flux density at $z = 0$ mm when $\bar{I} = 30$ A, $n = 8$, and the stator bore is empty.

After manufacturing the stator, the distribution of the magnetic flux density in the stator was measured with a Hall probe when the bore of the stator was empty. Root mean square (rms) values and instantaneous values of the magnetic flux density were measured with the Hall probe.

At first, the Lissajous figure was displayed on an oscilloscope from the instantaneous signal of the magnetic flux density and the primary current. Observation of the Lissajous figure for various locations and various angles of the probe confirmed the generation of the rotating twisted magnetic field.

Next, the magnetic flux density in a cross section was measured with the Hall probe. Table II shows circumferential averages of rms values of the measurement and a numerical analysis of the magnetic flux density in the central cross section $z = 0$ mm when $\bar{I} = 30$ A and $N = 8$. Both results are in good agreement and within the accuracy of the measuring instruments, except for the center.

Fig. 5 shows distribution of the measured rms values $\bar{B}_r$, $\bar{B}_\theta$ at $r = 20, 32$ mm and $z = 0$ mm. Measurement results show that the deviation of the spatial higher harmonics was within $\pm 6\%$ of the average. It was much smaller than the harmonics in the stator with teeth [7].

C. Molten Gallium Circulation System

In this experiment, we used molten gallium as the secondary conductor. The physical properties of gallium are shown in Table III [9].

TABLE III
PHYSICAL PROPERTIES OF GALLIUM

Atomic number	31
Atomic weight	69.72
Density [kg/m^3]	
323.15 [K] (Liquid)	6.08×10^3
Melting point [K]	302.91
Specific heat [J/(kg·K)]	
302.95 [K] (Liquid)	398
Thermal conductivity [W/(m·K)]	
302.95 [K] (Liquid)	25.5
Electric conductivity [S/m]	
303 [K] (Liquid)	3.86×10^6
Viscosity [Pa·s]	
323.15 [K] (Liquid)	1.93×10^{-3}

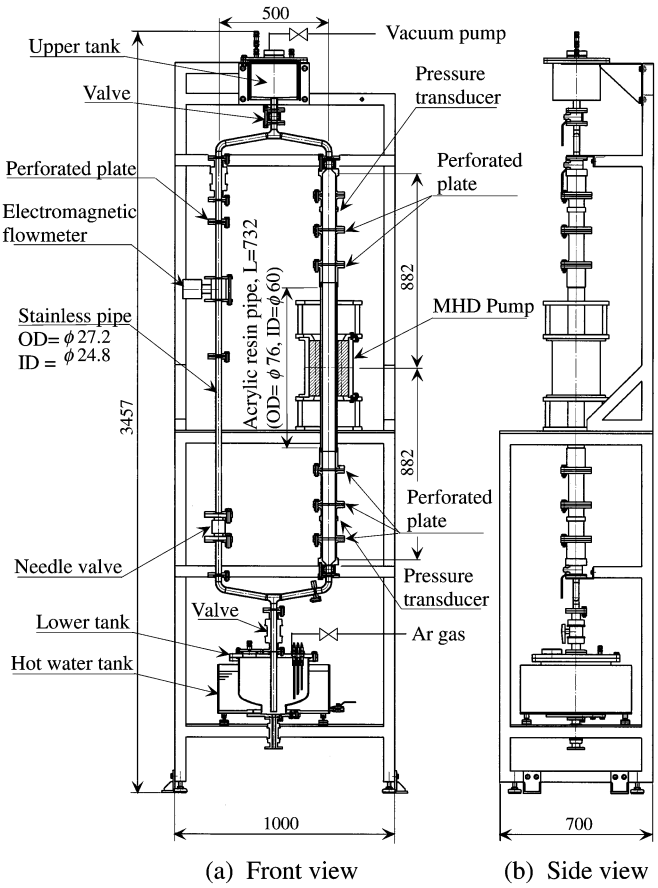

Fig. 6. Molten gallium circulation apparatus (unit: mm).

The molten gallium circulation apparatus is shown in Fig. 6. The gallium stored in lower tank is pushed up into the ducts by argon gas pressure. After the gallium filled the ducts, the valve under the upper tank was closed and the circulation experiment was performed.

This system consists of two kinds of ducts with different diameters. Therefore, before the experiment, we confirmed the hydrodynamic symmetry of this duct system: there was no difference between the upward and downward driving of the molten gallium. After this testing, we fixed the driving direction to be upwards.

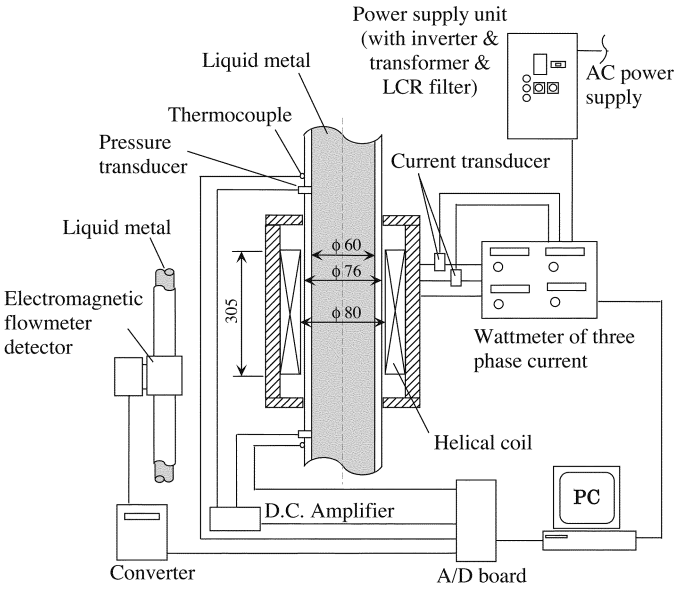

Fig. 7. Configuration of measurement system.

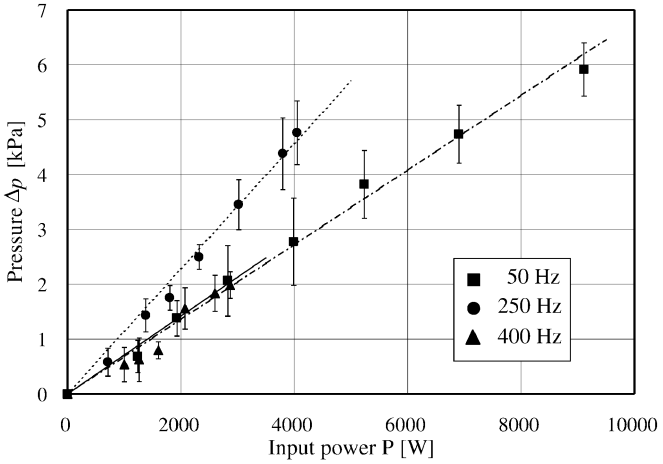

Fig. 8. Developed pressure for various input power.

TABLE IV
COEFFICIENT OF PRESSURE CURVE ON THE MOLTEN GALLIUM EXPERIMENT SHOWN IN FIG. 8

Frequency f [Hz]	α [Pa/W]
50	0.68
250	1.14
400	0.71

The rotating twisted magnetic field creates an axial flow with swirl. To eliminate the swirl effect on the pressure measurement, perforated plate conditioners with 35 holes are mounted in this duct system [10]. Four of the perforated plates are mounted in a symmetrical configuration with respect to the longitudinal center of the stator between the inlet and the outlet pressure transducer.

D. Measurement System

The measurement system is shown in Fig. 7. In this experiment, the flowrate, the inlet pressure, and the outlet pressure of the MHD pump were measured. The flowrate was measured with an electromagnetic flowmeter. Before the experiment, we calibrated this flowmeter using a volumetric method. The outputs of the flowmeter, the pressure transducers, and the wattmeter were sampled every 0.25 s and recorded on a personal computer.

IV. EXPERIMENTAL RESULTS

A. Pressure for Various Input Powers

The developed pressure Δp was measured for various input powers P, where Δp is defined as the difference in the static pressure between the outlet and inlet of the pump. This result is shown in Fig. 8. This experiment was performed at three frequencies: 50, 250, and 400 Hz. The needle valve in the duct system was at the full-open position. (Appendix II shows the P-Q curve, the developed pressure Δp as a function of the flowrate Q, obtained with various open states of this needle valve.) The error bar of the developed pressure shows the sample standard deviation. This result shows that the developed pressure is nearly proportional to the input power for each frequency

$$\Delta p = \alpha P. \tag{1}$$

The constant α of proportionality of each pressure curve is shown in Table IV. (There are some unstable values of about 0–1.6 kW for each frequency, as shown in Fig. 8. Therefore, values of α in Table IV were obtained from data at more than 1.6 kW.) Using α, we can extrapolate the input power to obtain any required pressure for each frequency.

Table IV shows the coefficient has a maximum at 250 Hz. This reason is that this frequency is very close to the characteristic frequency in this experiment. This detail is explained in Sections V and VI.

In Fig. 8, the maximum plotted points for each frequency are the maximum power limits of the power supply unit. Supplied current, voltage, and the power factor at the maximum power for each frequency are shown in Table V.

The efficiency of energy conversion was very low during this experiment (see Appendix III-A). The energy loss due to joule heating of the primary coil was a severe disadvantage to the efficiency of the energy conversion (see Appendix III-B). To discuss separately from this effect, we summarize the experimental data on the basis of the primary current rather than the input power, as shown in the following sections.

B. Flowrate and Pressure for Various Primary Currents

We rearranged the experimental data in Fig. 8 using the primary current as the horizontal axis. The developed pressure Δp and the flowrate Q versus the primary current $\bar{I}$ are shown in Figs. 9 and 10, respectively. The error bars of the flowrate cannot be distinguished in Fig. 10 because these sample standard deviations are very small, 0.08 L/min or less and of the same order as the accuracy of the electromagnetic flowmeter.

With respect to the flowrate curve at 50 Hz in Fig. 10, the gradient of the curve is not constant. This fact suggests that the velocity of the molten gallium, including the rotational speed,

TABLE V
MAXIMUM LIMIT VALUE OF THE POWER SUPPLY UNIT AND MEASUREMENT VALUES

Frequency f [Hz]	Current $\bar{I}$ [A]	Voltage $\bar{V}$ [V]	Power factor [%]	Power P [kW]	Flowrate Q [L/min]	Pressure Δp [kPa]
50	457	17.8	65	9.11	8.46 $\pm$0.3%	5.91 $\pm$8%
250	207	29.4	39	4.05	7.02 $\pm$0.7%	4.76 $\pm$12%
400	142	29.6	39	2.87	4.66 $\pm$0.9%	1.99 $\pm$12%

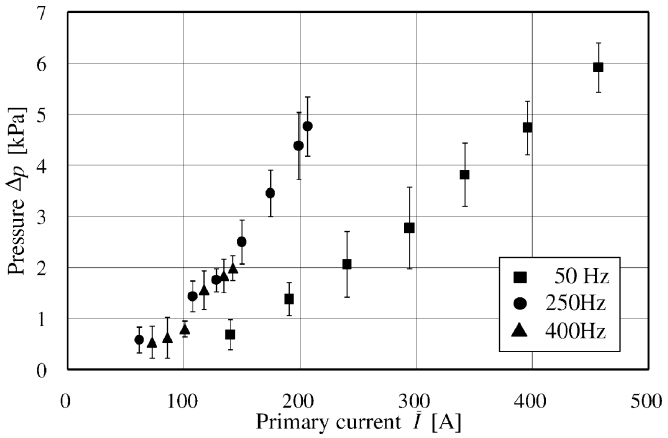

Fig. 9. Developed pressure for various primary currents.

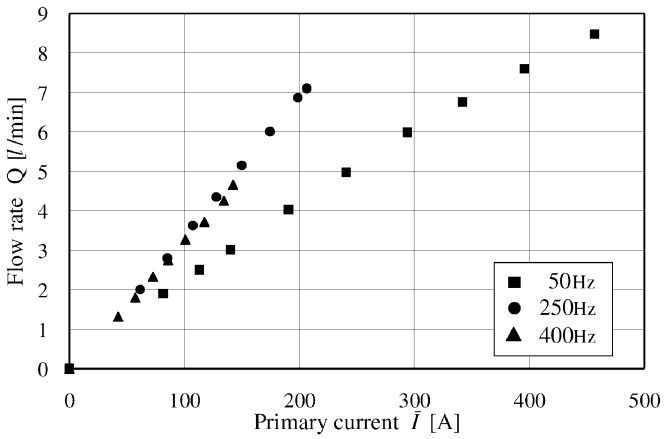

Fig. 10. Flowrate for various primary currents.

increases following the phase velocity of the magnetic field. This phenomenon will be discussed in detail in Section V.

The data in Figs. 9 and 10 are plotted on another graph, as shown in Fig. 11, where the horizontal axis is the flowrate Q and the vertical axis is the developed pressure Δp. This figure is the so-called load curve of the duct system. These data are plotted in the vicinity of a quadratic curve indicated by the dashed line in Fig. 11. This is a reasonable result because, from the viewpoint of the circulation duct system, the relationship between the flowrate and the pressure depends only on the pressure loss in the valves and the ducts except the part inserted in the pump. Thus, it does not depend on the frequency. The developed pressure Δp is a function of Q^2, and can be shown in

$$\Delta p = \beta Q^2 \text{ for fixed load.} \tag{2}$$

This is the Darcy–Weisbach friction loss equation [11].

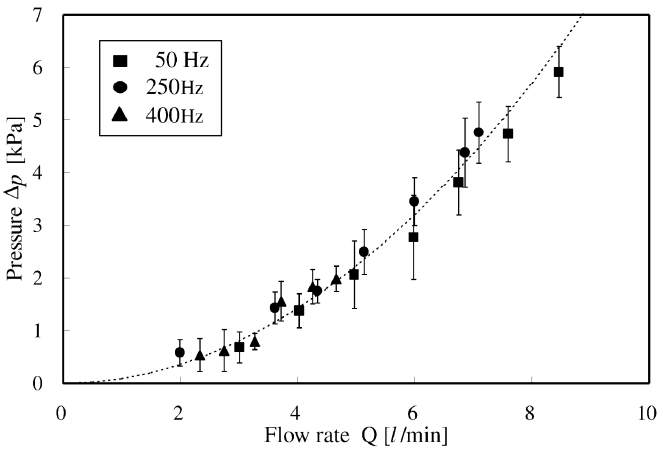

Fig. 11. Load curve by duct resistance with open needle valve.

In principle, the coefficient β is a function of the Reynolds number. However, since the measurement range of the flowrate is narrow in this experiment, we treat the coefficient β as a fixed constant. The coefficient β of our system is 89.1 Pa $\cdot$ min^2/L^2 at the full-open position of the needle valve.

V. SLIP OF MOLTEN GALLIUM

A. Discussion Based on the Conventional Slip-Thrust Relation

Our previous paper indicated that the slip-thrust curve of a solid secondary conductor can be expressed by a unique function applicable to any secondary conductor material, except ferromagnetic material [7]. According to that paper, the thrust F_z is given as follows:

$$\frac{F_z}{\bar{I}^2} = \mu_0 N^2 A_f \frac{2cR_\omega s}{1+(cR_\omega s)^2} \tag{3}$$

where N denotes the number of turns of coil windings, R_ω denotes the shielding parameter

$$R_\omega = 2\pi\sigma\mu_0 f {a_2}^2. \tag{4}$$

Here, σ denotes the conductivity of the secondary conductor, μ_0 denotes the space permeability, f denotes the frequency of power supply, and a_2 denotes the radius of the secondary conductor. The constants A_f and c in (3) are determined by comparing the curve with experimental data. The function (3) has a local maximum value $F_z/\bar{I}^2 = \mu_0 N^2 A_f$ at $cR_\omega s = 1$.

Slip s is a dimensionless parameter that explains the relative motion between the magnetic field and the secondary conductor. It is defined as

$$s = \frac{\omega - kU_z - \Omega}{\omega} \tag{5}$$

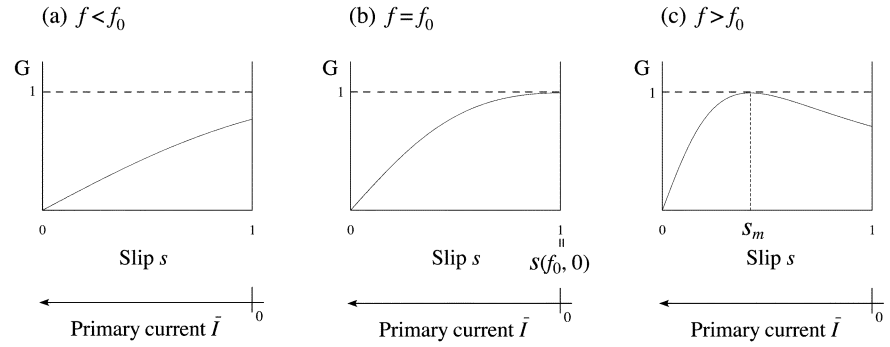

Fig. 12. Outlines of the slip-pressure function (9) for various frequency ranges: (a) $f < f_0$, (b) $f = f_0$, and (c) $f > f_0$.

where ω denotes the angular frequency of the rotating magnetic field, k denotes the wave number in the z direction, U_z and Ω denote the axial velocity in the z direction and the angular velocity of the secondary conductor, respectively. In the experiment using cylindrical solid metals, Ω was measured on the condition of $U_z = 0$ [7]. On the other hand, in this experiment using molten gallium, U_z was obtained from the flowrate, while Ω was not measured.

It is, by nature, expected that the relationship between the developed pressure Δp and slip of the molten gallium is similar to the relationship (3). Thus, the following relation is supposed for molten metal

$$\frac{\Delta p}{\bar{I}^2} = A_p \frac{2cR_\omega(f)s(f,\bar{I})}{1+\left\{cR_\omega(f)s(f,\bar{I})\right\}^2} \tag{6}$$

where $R_\omega(f)$ is a function of the frequency f, and $s(f,\bar{I})$ at steady state is a function of f and the primary current $\bar{I}$. The relation (6) gives the maximum value of a normalized developed pressure $\Delta p/\bar{I}^2 = A_p$ when $cR_\omega s = 1$. We call A_p "the normalized stalling pressure" after the stalling torque of induction motor.

We introduce a characteristic frequency f_0 for the experiment

$$cR_\omega(f_0) = 1. \tag{7}$$

The characteristic frequency f_0 corresponds to a local maximum of $\Delta p/\bar{I}^2$ when $\bar{I} \to 0$. In this condition, s is obtained as follows:

$$\lim_{\bar{I}\to 0} s = \lim_{U_z\to 0,\Omega\to 0} \frac{\omega - kU_z - \Omega}{\omega} = 1. \tag{8}$$

Consequently, the stalling condition $cR_\omega s = 1$ of (6) is satisfied when $f = f_0$ and $\bar{I} \to 0$.

By substituting (7) for (6) and dividing both sides of it by A_p, we obtain the following dimensionless slip-pressure function $G(f,\bar{I})$

$$G(f,\bar{I}) = \frac{2\frac{f}{f_0}s(f,\bar{I})}{1+\left\{\frac{f}{f_0}s(f,\bar{I})\right\}^2}. \tag{9}$$

Fig. 12 explains the outline of the slip-pressure function (9) for various frequency ranges. In general, slip s is a monotone decreasing function for the primary current $\bar{I}$. Therefore, we draw the graph for $0 \le s(f,\bar{I}) \le s(f,0) = 1$. In the case of $f < f_0$, there is no local maximum for $0 \le s \le 1$, as shown in Fig. 12(a). On the other hand, in the case of $f = f_0$, there is a local maximum at $s = 1$, as shown in Fig. 12(b). In the case of $f > f_0$, there is a local maximum at $s_m = f_0/f$, as shown in Figs. 12(c) and 13. Here, we name s_m the stalling slip.

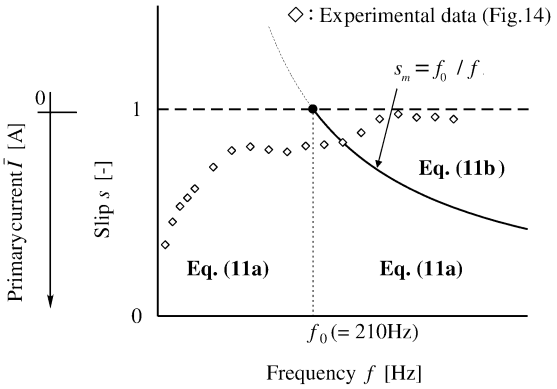

Fig. 13. Stalling slip $s_m = f_0/f$ and selection of two slip functions.

Because $s \to 1$ for $\bar{I} \to 0$, f_0 is obtained from (9) as follows:

$$f_0 = \frac{f}{G(f,0)}\left[1+\sqrt{1-G(f,0)^2}\right], \quad \text{for } f < f_0 \tag{10a}$$

$$f_0 = \frac{f}{G(f,0)}\left[1-\sqrt{1-G(f,0)^2}\right], \quad \text{for } f \ge f_0. \tag{10b}$$

If (6) is valid, all experimental data sets that are independent of one another give a unique value of f_0.

After deciding f_0, we obtain the slip s $(0 \le s \le 1)$ by (9). It is rearranged as follows:

$$s(f,\bar{I}) = \frac{1}{G(f,\bar{I})}\frac{f_0}{f}\left[1-\sqrt{1-G(f,\bar{I})^2}\right] \tag{11a}$$

$$s(f,\bar{I}) = \frac{1}{G(f,\bar{I})}\frac{f_0}{f}\left[1+\sqrt{1-G(f,\bar{I})^2}\right]. \tag{11b}$$

Fig. 13 explains the selection of two slip functions (11a) and (11b).

B. Verification of Slip-Pressure Function

If the supposed relation (6) is correct, the unique value of f_0 is obtained from any data set at an arbitrary frequency f. We try to verify this supposition using the results of the molten gallium experiment.

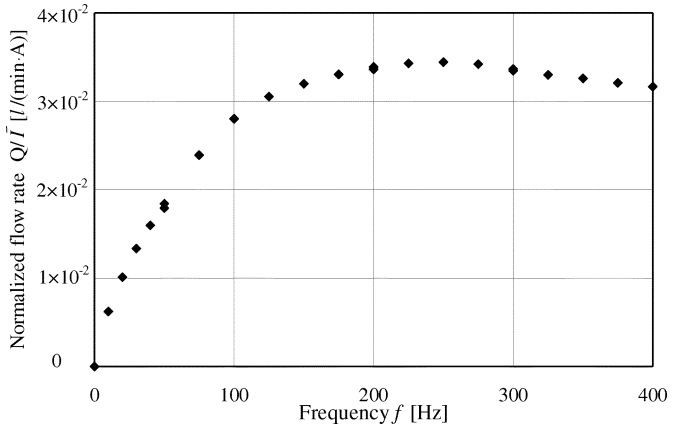

Fig. 14. Flowrate for various frequencies.

Here, we replace the developed pressure Δp with the flowrate Q by (2), because the accuracy of the experimental data of the flowrate is higher than that of the developed pressure

$$\left(\frac{Q}{\bar{I}}\right)^2 = \Lambda^2 G(f,\bar{I}) \text{ for fixed } \beta \tag{12}$$

where the constant Λ is the maximum value of a normalized flowrate $Q/\bar{I}$. The relation between A_p and Λ is

$$A_p = \beta\Lambda^2. \tag{13}$$

At first, to obtain the maximum value Λ in (12), the flowrate was measured for various frequencies. This result is shown in Fig. 14. The vertical axis is the normalized flowrate $Q/\bar{I}$. In this experiment, the maximum value of $Q/\bar{I}$ is $\Lambda = 3.44 \times 10^{-2}$ L/(A · min) when $f = 250$ Hz and $\bar{I} = 195$ A.

Next, we need to obtain $G(f,0)$. The value of $G(f,0)$ can be interpreted as follows:

$$G(f,0) = \frac{1}{\Lambda^2}\left[\lim_{\bar{I}\to 0}\frac{\partial Q}{\partial \bar{I}}\right]^2. \tag{14}$$

To obtain $G(f,0)$ by (14), we calculated approximate curves of three experimental data sets plotted in Fig. 10. This result is shown in Table VI. Polynomial expressions to second-order shown in Table VI are enough to obtain the gradient of each curve for $\bar{I} \to 0$. The coefficients of determination in Table VI are $R^2 \geq 0.999$.

The approximate curves in Table VI give $G(f,0)$. Moreover, f_0 are derived from (10a) or (10b). Each value of f_0 obtained from these data sets is between 207 and 210 Hz and almost the same frequency, as shown in Table VI. It is verified that the supposed equation (6) is satisfied in this experiment with molten metal. The form of (6) suggests that (6) is applicable to any molten metal.

As shown in Table VI, a first-order function is adopted as the approximate curve for 250 Hz. In Fig. 10, the plotted data for 250 Hz is close to linear. More careful observation shows that the plotted points fit an S-shaped curve. This fact shows that the curve drawn from these data has a point of inflection, at which the slip is s_m because $Q/\bar{I}(\simeq \partial Q/\partial \bar{I})$ is a maximum. These facts suggest that there is frequency f_0 in the neighborhood of 250 Hz. In this case, the number of data points and the accuracy are not enough to adopt a higher order approximate curve. Therefore, the first-order function is adopted in the case of 250 Hz.

C. Identification of the Slip

Substituting experimental value of $G(f,\bar{I}) = Q^2/(\bar{I}\Lambda)^2$ for (11a) or (11b), we obtain each slip s for each condition. Fig. 15 shows the slip s of each experimental data point plotted in Fig. 10, where $f_0 = 210$ Hz is adopted. The horizontal axis is the slip s and the vertical axis is $(Q/\bar{I})^2$. Slips s within the region of $0 \leq s \leq 1$ are plotted in this figure. As a matter of fact, there are four rejected points of 250 Hz. Solid lines drawn by (12) are added to Fig. 15.

Similarly, slips of the plotted data in Fig. 14 are calculated and shown in Fig. 13.

VI. Discussion

A. Motion of Molten Gallium

By substituting each slip in Fig. 15 for (5), we obtain the angular velocity of the molten gallium, as shown in Fig. 16. The results at 50 and 250 Hz show that the rotational speed increases with the flowrate. However, the result at 400 Hz shows that the rotational speed does not always increase. We suspect that the motion of the molten metal is unstable in the case of 400 Hz. It is well known that similar unstable operation of ordinary induction motors occurs when the slip is higher than the stalling slip s_m. In Fig. 15, all the slip values in the case of 400 Hz are higher than $s_m \simeq 0.5$.

The maximum angular velocity $\Omega_{\max}$ at 50 Hz is 118 rad/s ($s_{\min} = 0.62$). The circumferential component U_θ of velocity at the outer edge of the boundary layer on the duct wall is estimated to be 3.55 m/s. It is 71 times as large as U_z. Hence, the motion in the axial direction contributes 0.8% of all the slip. Similarly, $\Omega_{\max}$ at 250 Hz is 376 rad/s ($s_{\min} = 0.76$). Thus, U_θ is 11.3 m/s. The motion in the axial direction contributes 0.2% of all the slip. So, the rotational velocity of molten gallium accounts for almost all of the slip in this experiment. This excessive rotational velocity has to be reduced in future improved design of the pump system.

B. Skin Depth

The skin depth δ of a rotational secondary conductor is given as follows (see [12]):

$$\delta = \sqrt{\frac{1}{\mu_0\sigma\pi f s}}. \tag{15}$$

When $\Delta p/\bar{I}^2$ is equal to the normalized stalling pressure A_p, the stalling skin depth δ_m is given by substituting $s = s_m = f_0/f$ for (15)

$$\delta_m = \sqrt{\frac{1}{\mu_0\sigma\pi f_0}}. \tag{16}$$

Substituting $f_0 = 210$ Hz and the conductivity of gallium for (16), we obtain

$$\frac{\delta_m}{a_2} = 0.59. \tag{17}$$

TABLE VI
APPROXIMATE EXPRESSIONS OF FLOWRATE, $G(f,0)$ AND f_0 DERIVED FROM THE MOLTEN GALLIUM EXPERIMENT

Frequency f	Approximate expression of flowrate§	Coefficient of determination	$G(f,0)$†	f_0‡
[Hz]	[L/min]	[-]	[-]	[Hz]
50	$Q = -1 \times 10^{-5}\bar{I}^2 + 0.0231\bar{I}$	R^2 = 0.9999	4.51 $\times 10^{-1}$	210
250	$Q = 0.0341\bar{I}$	R^2 = 0.9991	9.83 $\times 10^{-1}$	207
(250)	$(Q = 1 \times 10^{-5}\bar{I}^2 + 0.0323\bar{I})$	(R^2 = 0.9998)	(8.82 $\times 10^{-1}$)	(150)
400	$Q = 7 \times 10^{-6}\bar{I}^2 + 0.0312\bar{I}$	R^2 = 0.9991	8.23 $\times 10^{-1}$	210

§given by Fig. 10, †given by (14), ‡given by (10a) or (10b).

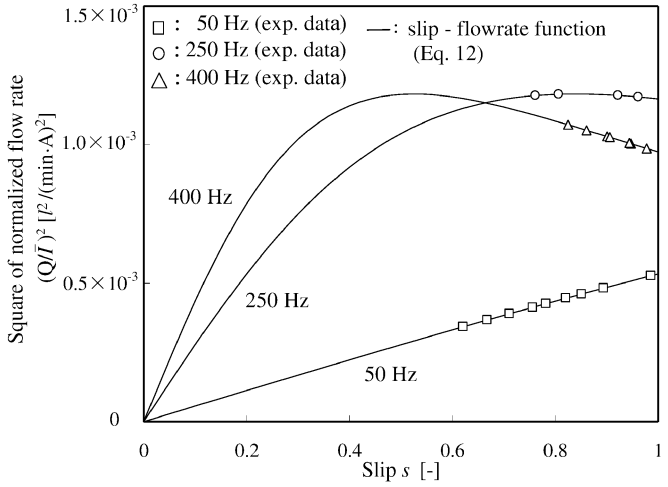

Fig. 15. Slip-flowrate curves ($f_0 = 210$ Hz).

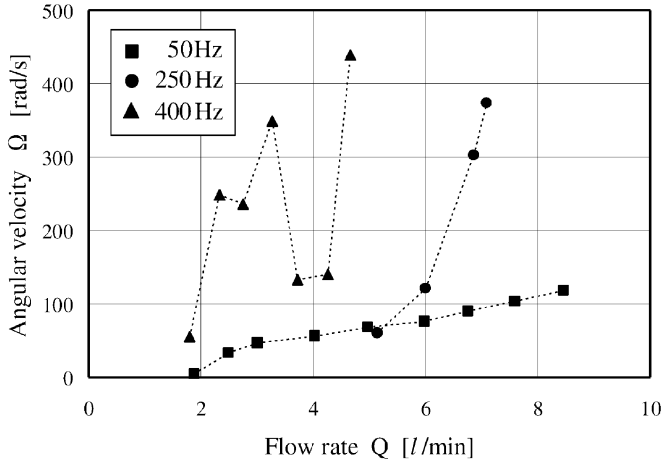

Fig. 16. Rotational speed for each flowrate data ($f_0 = 210$ Hz).

In consideration of the electromagnetic similarity, this relationship is expected to have universality and not depend on the size of the device nor the motion nor the material property of the secondary conductor.

In the previous experiment using cylindrical solid conductors, $\delta_m/a_2 \simeq 0.5$ was obtained [7]. The value of δ_m/a_2 for molten metal is larger than that for solid metal. This is a reasonable result because the liquid secondary conductor requires uniform thrust to a certain extent, while the solid secondary conductor accepts nonuniform thrust.

C. Twist Angle of Coil

Penetration of the magnetic field is decided by the skin depth and twist angle of the coil. Even if the skin depth is greater than the duct diameter, too large a twist angle results in a lack of magnetic field at the center of the secondary conductor. The magnetic field generated by the helical coil of this experiment sufficiently penetrates the center if the skin effect is negligible, for example, $s = 0$ [7]. Meanwhile, since $\delta_m/a_2 \simeq 0.6$, it is not necessary that the magnetic field fully penetrates the center of the secondary conductor. Consequently, we have a certain design flexibility with respect to the twist angle of the coil. Section VI-A indicates that the Lorentz force produces the rotational velocity rather than the axial velocity, and the former accounts for almost all of the slip. Therefore, the optimum twist angle of coil is larger than the present twist angle (39°).

VII. REQUIREMENT FOR USING HIGH-TEMPERATURE MOLTEN METAL

Our induction pump aims at material processing, for example, molten steel at over 1500 °C or highly reactive metal. Therefore, performance in a harsh environment is required for this MHD pump [13]. In principle, there is no problem for this MHD pump. However, at the present time, there are the following requirements.

- Fail-safe design to prevent a leakage of cooling water from the copper pipe of the helical coil.
- The establishment of an insulating shield to prevent a temperature rise of the stator and temperature fall of the molten metal.
- The improvement in the heat resistance of the stator.

In the future, we must attempt to improve the efficiency and meet these requirements.

VIII. CONCLUSION

An electromagnetic induction pump that gives thrust to high-temperature molten metal in a cylindrical duct is studied. This paper reports on a circulation experiment using molten gallium as the secondary conductor. The following results were obtained from this experiment.

1) A stator without teeth or slots was fabricated for this experiment. Uniformity of the magnetic flux density was remarkably improved. Measurement results of the magnetic flux density show that the deviation was within $\pm 6\%$ of the average, and the effect of spatial higher harmonics was suppressed.

2) The developed pressure is nearly proportional to the input power.
3) It is confirmed that the conventional slip-thrust function is valid for the results of this experiment with molten gallium. The form of this function suggests that it is applicable to any molten metal.
4) These experimental results show that the normalized stalling pressure was obtained when the ratio of the skin depth to the radius of the secondary conductor is 0.59. In consideration of the electromagnetic similarity, this relationship is expected to have universality and not depend on the size of the device nor the motion nor the material property of the secondary conductor.
5) The rotational velocity was much greater than the axial velocity, and the former accounted for almost all of the slip. This excessive rotational velocity has to be reduced in future improved design of the pump system.
6) The optimum twist angle of the coil is larger than the present twist angle (39°).

Appendix I
Magnetic Field Analysis

Numerical analysis of the magnetic flux density without secondary conductor was performed to confirm the difference between stators with and without teeth.

A. Distribution of the Magnetic Flux Density of a Rotating Twisted Magnetic Field

Gauss's law in cylindrical coordinates is shown as follows:

$$\frac{1}{r}\frac{\partial(rB_r)}{\partial r}+\frac{1}{r}\frac{\partial B_\theta}{\partial\theta}+\frac{\partial B_z}{\partial z}=0. \tag{18}$$

In the case of a twisted magnetic field, independent variables are transformed as follows:

$$T=t,\quad R=r,\quad \Theta=\theta+kz-\omega t,\quad Z=z \tag{19}$$

where k denotes the wave number in the z direction. Here, we use the following two assumptions. The end effect is negligible: $\partial/\partial Z=0$ for all variables. A steady state is established: $\partial/\partial T=0$. Equation (18) is rewritten from (19) and using the above assumptions

$$\frac{1}{R}\frac{\partial(RB_r)}{\partial R}+\frac{1}{R}\frac{\partial}{\partial\Theta}\left(B_\theta+kRB_z\right)=0. \tag{20}$$

The following magnetic flux density vector automatically satisfies (20)

$$\begin{aligned}B_r&=\frac{1}{R}\frac{\partial A}{\partial\Theta}\\ B_\theta&=-\frac{1}{1+k^2R^2}\frac{\partial A}{\partial R}\\ B_z&=-\frac{kR}{1+k^2R^2}\frac{\partial A}{\partial R}.\end{aligned} \tag{21}$$

Considering the actual coil shape, the current density in the windings are given by

$$j_\theta+kRj_z=0,\quad j_r=0. \tag{22}$$

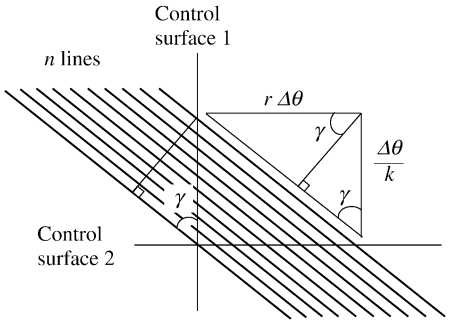

Fig. 17. Coil current about one phase; expansion plan at radius r.

Equation (22) satisfies Kirchhoff's law ($\nabla\cdot\boldsymbol{j}=0$)

$$\frac{1}{R}\frac{\partial}{\partial R}\left(Rj_r\right)+\frac{1}{R}\frac{\partial}{\partial\Theta}\left(j_\theta+kRj_z\right)dR=0. \tag{23}$$

Ampére's law is

$$\begin{aligned}\frac{1}{R}\frac{\partial H_z}{\partial\Theta}-k\frac{\partial H_\theta}{\partial\Theta}&=0\\ k\frac{\partial H_r}{\partial\Theta}-\frac{\partial H_z}{\partial R}&=j_\theta\\ \frac{1}{R}\frac{\partial}{\partial R}\left(RH_\theta\right)-\frac{1}{R}\frac{\partial H_r}{\partial\Theta}&=j_z.\end{aligned} \tag{24}$$

Taking $\boldsymbol{B}=\mu\boldsymbol{H}$ into account, we obtain the same equation from the second and third equations of (24)

$$\frac{1}{R}\frac{\partial}{\partial R}\left\{\frac{R}{\mu(1+k^2R^2)}\frac{\partial A}{\partial R}\right\}+\frac{1}{R^2}\frac{\partial}{\partial\Theta}\left(\frac{1}{\mu}\frac{\partial A}{\partial\Theta}\right)=-j_z \tag{25}$$

where μ denotes the magnetic permeability. The first equation of (24) is automatically satisfied. Equation (25) is calculated by the finite difference method, where μ is a given function of R and Θ.

B. Helical Coil Current

Here, we derive the relationship between the coil current and the current density j_z inside the winding model of the numerical analysis.

If the diameter of the windings is D, in Fig. 17

$$nD=\frac{\Delta\theta}{k}\sin\gamma \tag{26}$$

where $r\Delta\theta$ denotes the width of windings per one-phase and one-pole slot-width of the yoke when the stator has teeth. The angle $\Delta\theta$ is $\pi/3$ in the case of the stator without teeth. On the other hand, $\Delta\theta$ is $\pi/6$ in the case of the stator with teeth (see [7]).

When the current per winding is $\bar{I}$, the current per area of thickness dr about one phase is

$$n\frac{dr}{D}\bar{I}=\frac{\bar{I}dr}{D^2}\frac{\Delta\theta}{k}\sin\gamma. \tag{27}$$

The current, which flows through a control surface, is shown

$$\int\boldsymbol{j}\cdot\boldsymbol{n}dS \tag{28}$$

TABLE VII
NUMERICAL RESULTS OF MAGNETIC FLUX DENSITY

Way of winding	Teeth of yoke	Current density [A/m^2]	Magnetic flux density [mT]				Result of analysis
			B_y			B_z	
			Center	Right wall	Upper wall	Right wall	
Three-phase concentrated-winding	With teeth	2×10^6	22.5	42.9	39.4	42.9	Fig. 18
Three-phase distributed-winding	Without teeth	2×10^6	27.4	31.6	43.5	31.6	Fig. 19

where $\boldsymbol{j}$, $\boldsymbol{n}$, and dS denote a current density vector, a normal vector for the control surface, and the area element in the control surface, respectively. The integrals (28) for both control surfaces 1 and 2 are equal to (27)

$$-\frac{\bar{I}dr}{D^2}\frac{\Delta\theta}{k}\sin\gamma = j_\theta\frac{\Delta\theta}{k}dr$$
$$\frac{\bar{I}dr}{D^2}\frac{\Delta\theta}{k}\sin\gamma = j_z r\Delta\theta dr \tag{29}$$

where, on the right-hand side of the equations, the current density across the control surface is regarded as uniform irrespective of the gap in the windings.

Substituting $J=\bar{I}/D^2$ and $\sin\gamma = kr/\sqrt{1+k^2r^2}$ for (29), we obtain

$$j_\theta = -\frac{kr}{\sqrt{1+k^2r^2}}J, \quad j_z = \frac{1}{\sqrt{1+k^2r^2}}J \tag{30}$$

where J denotes the magnitude of the current density. The actual magnitude of the current density is $4\bar{I}/(\pi D^2)$ when the cross section of the winding is a circle. However, we adopt the current density $J=\bar{I}/D^2$ in the numerical analysis to distribute it uniformly irrespective of the gap in the windings.

The current through an area of radius r and thickness dr is

$$j_z r\Delta\theta\, dr = \frac{rJ}{\sqrt{1+k^2r^2}}\Delta\theta\, dr. \tag{31}$$

Integrating (31) by $R_0 \le r \le R_1$, we obtain

$$N\bar{I} = \frac{J\Delta\theta}{k^2}\left(\sqrt{1+k^2{R_1}^2}-\sqrt{1+k^2{R_0}^2}\right) \tag{32}$$

where N denotes the number of turns of the coil per phase and per pole. Though the current $N\bar{I}$ of an ordinary coil is proportional to $\left[{R_1}^2-{R_0}^2\right]$, the current of a helical coil is not proportional to the increase in radius, as shown in (32).

In the previous experiment [7], the inside and the outside radius of the stator were $R_0=0.04$ m and $R_1=0.059$ m, respectively. The wave number in the z direction was $k=25$ m^{-1}, where the twist angle was 45°, and the angle of the slot-width of the stator was $\Delta\theta\simeq\pi/6$. The number of turns of the windings per phase was $N=50$. Therefore, the current density J is obtained from (32)

$$\bar{I} = 6.16\times10^{-6}J. \tag{33}$$

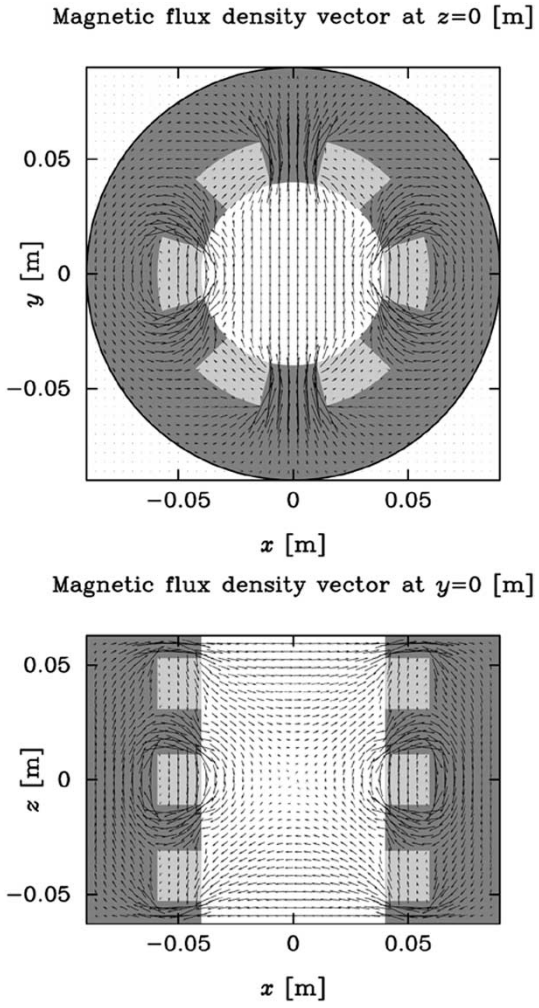

Fig. 18. Three-phase concentrated winding with six teeth.

C. Analysis Result

We analyze the magnetic flux density in two type of stators at $\bar{I}=12.3$ A$(J=2\times10^6$ A/m$^2)$. In this case, the magnetic permeability of the yoke is 1001 μ_0 and that of the other part is μ_0. The result is shown in Table VII. In the case of the three-phase concentrated winding, which was used in the previous experiment [7], the stator has six teeth and six slots. In the case of the three-phase distributed winding, the stator does not have teeth or slots.

The numerical result shows that the magnetic flux density at the center of three-phase distributed-winding is larger than that of a three-phase concentrated winding. Comparing Fig. 19 with Fig. 18, we can see that Fig. 19 is more uniform than Fig. 18.

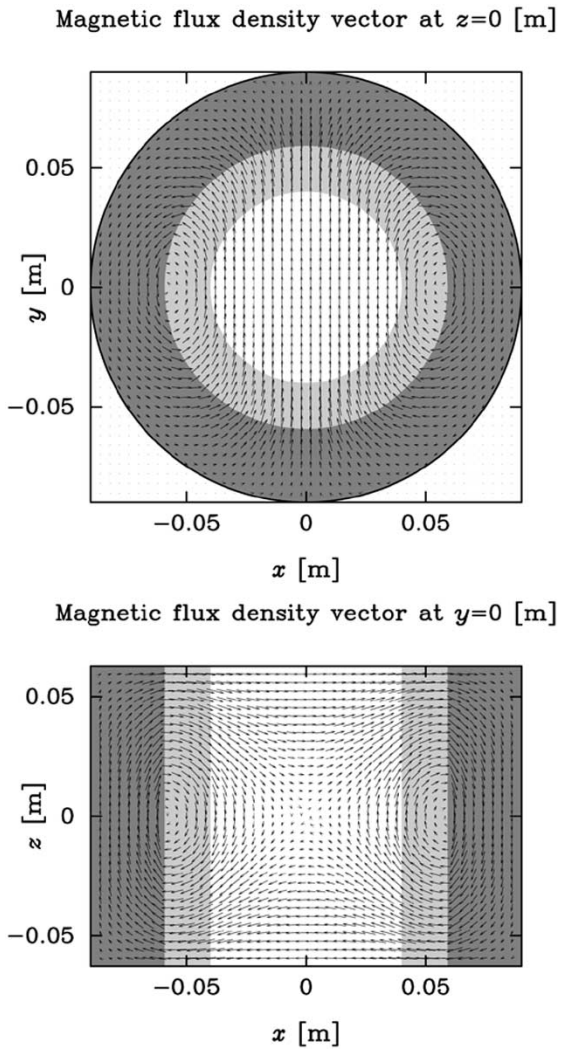

Fig. 19. Three-phase distributed winding without teeth.

APPENDIX II
PRESSURE-FLOWRATE CHARACTERISTIC

The pressure-flowrate characteristic of our MHD pump is shown in Fig. 20. This figure shows two results at 50 and 250 Hz where each current (phase current) was 457 and 206 A, respectively. The line voltage and power factors were 18 V, 65% at 50 Hz and 29 V, 39% at 250 Hz and were almost constant throughout the measurements.

This measurement has been performed for various open states of the needle valve. The maximum flowrate points $(**)$ of each frequency in Fig. 20 were measured by replacing the needle valve with a straight duct. These experimental results show that the obtained developed pressure barely changes with flowrate. Therefore, for both frequencies, the efficiency increases with flowrate.

APPENDIX III
ENERGY CONVERSION

A. Developed Mechanical Power and Efficiency

The developed mechanical power and the efficiency of our MHD pump were examined with open needle valve. The output power $Q\Delta p$ and the efficiency η for various input powers P are shown in Fig. 21. The efficiency at 250 Hz is the best among

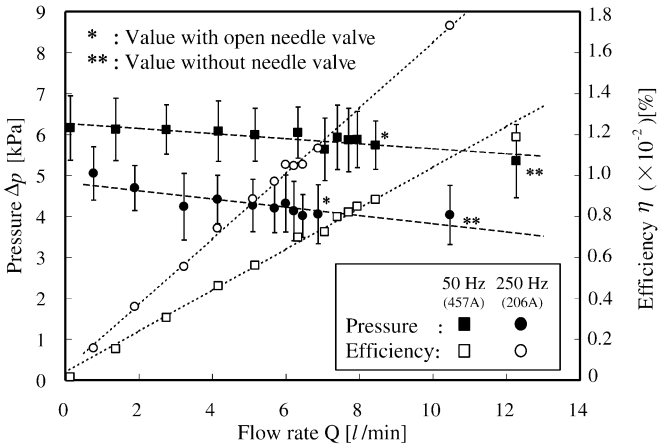

Fig. 20. Pump characteristics.

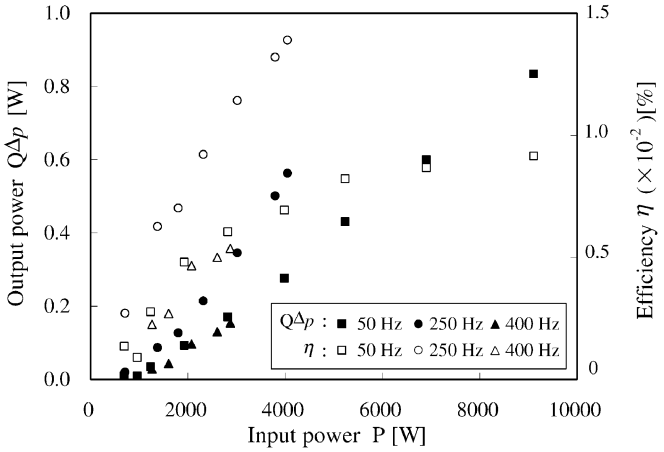

Fig. 21. Relationship between P and $Q\Delta p$ with open needle valve.

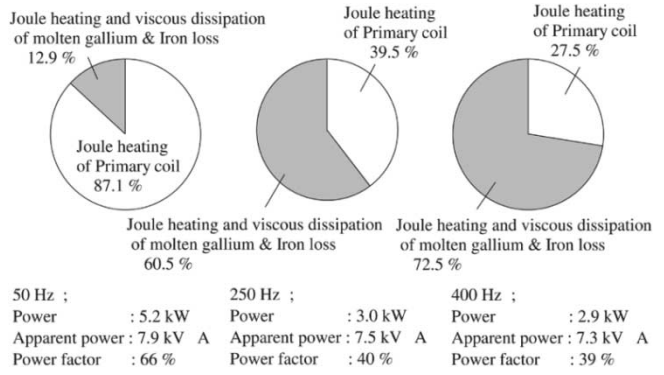

Fig. 22. Ratio of joule heating on output.

these three kinds of experiments, 50, 250, and 400 Hz. The efficiency increases with the input power. However, at about 50 Hz, the rising rate of efficiency becomes smaller with the input power. The efficiencies at the other frequencies show the same tendency. The efficiency of our MHD pump (of the order of 0.01%) is of three orders smaller efficiency than that of annular linear type MHD pump (of the order of 30%–40%) [4].

B. Joule Heating in the Primary Coil

We examine the joule heating of the primary coil from the electric resistance and the current for each phase in this experiment. Typical ratios of joule heating are shown in Fig. 22 at

almost the same apparent power at each frequency. We get the values of joule heating and viscous dissipation in the molten gallium and the iron loss in the yoke by subtracting the joule heating of the primary coil from the input power.

The result at 50 Hz indicates that about 90% of the input power is dissipated as joule heating in the primary coil. This ratio decreases as the frequency increases. The suppression of joule heating in the primary coil is a very important problem.

ACKNOWLEDGMENT

The authors would like to thank Dr. H. Arazeki of the Central Research Institute of Electric Power Industry for helpful discussions on the annular linear induction pump and Prof. K. Amagai of Gunma University and T. Sato of the Institute of Fluid Science, Tohoku University, for help with the detailed design of our experimental equipment. J. Fukuda of Nippon Steel Company is also thanked for helpful discussions on the application to material processing and Prof. K. Sawada of Tohoku University for help with this whole study.

REFERENCES

[1] M. Garnier, "Technological and economical challenges facing EPM in the next century," in *Proc. Int. Symp. Electromagnetic Processing of Materials*, 2000, pp. 3–8.

[2] T. Fujii, "State of art electromagnetic processing in Japanese iron and steel industry," in *Proc. Int. Symp. Electromagnetic Processing of Materials*, 2000, pp. 14–19.

[3] L. R. Blake, "Conduction and induction pumps for liquid metals," in *Proc. Inst. Elect. Eng.*, 1956, pp. 49–63.

[4] H. Arazeki, I. R. Kirillov, G. V. Preslitsky, and A. P. Ogorodnikov, "Double-supply-frequency pressure pulsation in annular linear induction pump, part II: Reduction of pulsation by linear winding at both stator ends," *Nucl. Eng. Des.*, vol. 195, pp. 397–406, 2000.

[5] S. V. Vasil'ev and A. I. Kozlov, "Electromagnetic phenomena in a cylindrical linearly helical induction pump," *Magnetohydrodynamics*, no. 4, pp. 87–94, 1972.

[6] K. Ueno, T. Ando, S. Taniguchi, and T. Takagi, "Axial driving force induced by rotating twisted magnetic field," in *Proc. Int. Symp. Electromagnetic Processing of Materials*, 2000, pp. 491–496.

[7] T. Ando, K. Ueno, S. Taniguchi, and T. Takagi, "Induction pump for high-temperature molten metals using rotating twisted magnetic field: Thrust measurement experiment with solid conductors," *IEEE Trans. Magn.*, vol. 38, pp. 1789–1796, July 2002.

[8] ——, "Visual system experiment of MHD pump using rotating twisted magnetic field applicable to high-temperature molten metals," *ISIJ Int.*, vol. 43, pp. 849–854, 2003.

[9] *Smithells Metals Reference Book*, 7th ed., E. A. Brandes and G. B. Brook, Eds., Butterworth-Heinemann, London, U.K., 1992.

[10] K. Akashi *et al.*, *Proc. IMEKO Symp. Flow Measurement and Control in Industry*, Tokyo, Japan, 1979, p. 279.

[11] F. M. White, *Fluid Mechanics*, 2nd ed. New York: McGraw-Hill, 1986, p. 303.

[12] S. Yamamura, *Theory of Linear Induction Motors*. Tokyo, Japan: Univ. Tokyo Press, 1978, p. 91.

[13] T. S. Jones, S. Ramachandran, W. B. Yerrick, and J. W. Gahan, "Development and testing of an experimental electromagnetic pump for liquid steel," *Metallurg. Trans.*, vol. 2, pp. 433–436, 1971.